

# Comprehensive Robotic Cholecystectomy Dataset (CRCD)<sup>†</sup>: Integrating Kinematics, Pedal Signals, and Endoscopic Videos

Ki-Hwan Oh<sup>1\*</sup>, Leonardo Borgioli<sup>1\*</sup>, Alberto Mangano<sup>2</sup>, Valentina Valle<sup>2</sup>, Marco Di Pangrazio<sup>3</sup>, Francesco Toti<sup>4</sup>, Gioia Pozza<sup>5</sup>, Luciano Ambrosini<sup>2</sup>, Alvaro Ducas<sup>2</sup>, Miloš Žefran<sup>1</sup>, Liaohai Chen<sup>2</sup> and Pier Cristoforo Giulianotti<sup>2</sup>

**Abstract**—In recent years, the potential applications of machine learning to Minimally Invasive Surgery (MIS) have spurred interest in data sets that can be used to develop data-driven tools. This paper introduces a novel dataset recorded during ex vivo pseudo-cholecystectomy procedures on pig livers, utilizing the da Vinci Research Kit (dVRK). Unlike current datasets, ours bridges a critical gap by offering not only full kinematic data but also capturing all pedal inputs used during the procedure and providing a time-stamped record of the endoscope’s movements. Contributed by seven surgeons, this data set introduces a new dimension to surgical robotics research, allowing the creation of advanced models for automating console functionalities. Our work addresses the existing limitation of incomplete recordings and imprecise kinematic data, common in other datasets. By introducing two models, dedicated to predicting clutch usage and camera activation, we highlight the dataset’s potential for advancing automation in surgical robotics. The comparison of methodologies and time windows provides insights into the models’ boundaries and limitations.

## I. INTRODUCTION

The training of state-of-the-art models requires the development of extensive datasets. In recent years, considerable efforts have been made to establish sizable public datasets for surgical procedures, featuring comprehensive annotations from experts. The creation of extensive data sets specifically focused on the execution of surgical tasks using robotic systems is an important step toward furthering these advances. The datasets offer a comprehensive portrayal of the surgeon’s actions, encompassing both kinematic and dynamic data, alongside recorded videos.

Most of the data sets focus on segmentation of the instruments [1], [2] and/or organs [3]–[5] captured by the endoscope during surgical procedures. For example, [6] is a video data set with instrument segmentations that also includes the labeling of different phases of the cholecystectomy (surgical

removal of the gallbladder) procedure (similar to Section III-B), and was used to train EndoNet [6] which predicts the presence of instruments and recognizes the current surgical phase. However, these datasets do not include kinematic data. This makes it difficult to estimate the 3D position of the detected instrument and calculate its distance to the tissues. Moreover, kinematic data has been reported to help improve tool segmentation [7], [8].

Few state-of-the-art datasets include kinematic data, as illustrated in [9]. For example, in [10], they recorded the kinematics of the controllers and the surgical robot arms while recording the video from non-endoscopic stereo cameras. However, the cameras were in a fixed location, and the way the images were captured was different from what was shown in endoscopic videos. In addition, they performed basic training tasks such as moving a peg or following a wire on a board, as opposed to real surgical procedures. More advanced tasks such as suturing and knotting were performed on the JIGSAWS [11] dataset, but it was a toy experiment and not applied to real tissues. In [12], kinematics was recorded, but it was only used to improve the instrument segmentation data set to be more robust with respect to different background tissues, and the movements were not related to surgical procedures.

In addition, one of the significant but trivial interaction signals is ignored in the existing datasets, which are the pedals of the robot surgery system. Surgeons frequently use the pedals to stop the robot arms and move the endoscope, and to apply mono/bipolar power to the instrument to dissect tissues. Analyzing these interactions and automating these secondary tasks is the key to alleviating the stress and burden on surgeons during prolonged surgical interventions.

To address the shortcomings observed in the previously released datasets, we decided to record cholecystectomy procedures using a coupled set of videos, kinematics data, and pedal signals. Cholecystectomy was chosen since it is one of the popular and standard laparoscopic procedures [13], [14]. The same applies to robotic cholecystectomy which has been gradually (mainly due to perceived higher costs) increasing in popularity [15]. The robotic cholecystectomy procedures are similar to the laparoscopic approach, and the details of the procedure are described in Section III.

<sup>†</sup> [https://github.com/Borgioli/crcd\\_ros.git](https://github.com/Borgioli/crcd_ros.git)

\* First two authors contributed equally to this work.

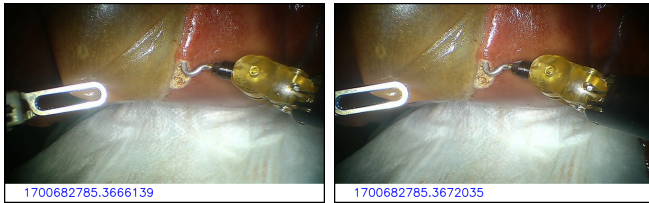
<sup>1</sup> Robotics Lab, Department of Electrical and Computer Engineering, College of Engineering, University of Illinois Chicago, Chicago, IL 60607, USA.

<sup>2</sup> Surgical Innovation and Training Lab, Department of Surgery, College of Medicine, University of Illinois Chicago, Chicago, IL 60607, USA.

<sup>3</sup> School of Medicine and Surgery, University of Modena and Reggio Emilia, Modena, Italy.

<sup>4</sup> Department of Medicine and Surgery, University of Milan, Milano, Italy.

<sup>5</sup> Department of Surgery, Lugano Regional Hospital, Ente Ospedaliero Cantonale (EOC), Lugano, Switzerland.



(a) Left endoscope. (b) Right endoscope.

Fig. 1: Sample of the stereo endoscopic images.

## II. DATASET COMPOSITION

### A. Stereo Endoscopic Images

This study utilizes the first-generation da Vinci surgical system integrated with the dVRK. In contrast to traditional configurations, we selected the Si model endoscope due to its superior image quality and significantly reduced noise characteristics. The stereo endoscope cameras are calibrated as described in OpenCV [16], based on the approaches presented in [17] and [18], finding the intrinsic and extrinsic parameters for each camera. The dataset includes distortion parameters, intrinsic camera matrix, rectification matrix, and projection matrix for the left and right endoscopes. These parameters facilitate the recovery of 3D point clouds from the recorded videos.

Individual images from each camera are recorded separately, featuring an additional timestamp placed at the bottom of the image, as illustrated in Fig. 1. The timestamps are from the Robot Operating System (ROS) [19] and can be extracted utilizing optical character recognition (OCR) engines such as the Tesseract [20]. With these timestamps, one could find the corresponding kinematics and pedal signals from the dataset. Each video was recorded with a rate of 60 frames per second and a resolution of  $1280 \times 720$  pixels. The videos are encoded in AVC1 four-character code (FourCC) and compressed to MP4 files for minimum size.

### B. Pedals

The pedals of our current da Vinci model consist of *camera*, *clutch*, *monopolar*, and *bipolar* functionalities. However, the dVRK provides the pedal signals solely at the moment when the pedals are pressed. Consequently, to achieve synchronization with the image and kinematic data, we interpolated the signals for the camera and clutch pedals, where the signals are 0 by default and remain 1 while the pedal is pressed. This interpolation ensures coherence across the image and kinematic data.

Moreover, the dVRK lacks direct control over the electro-surgical generator (or electro-surgical unit, ESU) responsible for regulating the voltage output of the monopolar instruments used for tissue dissection. In our setup, the Pfizer Valleylab Force 2 electro-surgical generator was used, where its input schematic remained a black box. However, we discovered that a minimum current of  $1mA$  must flow through the input cable originally connected to the pedals to activate the monopolar output of the generator. To address this, we established an interface between the generator's input cable and the da Vinci console pedals using an Arduino,

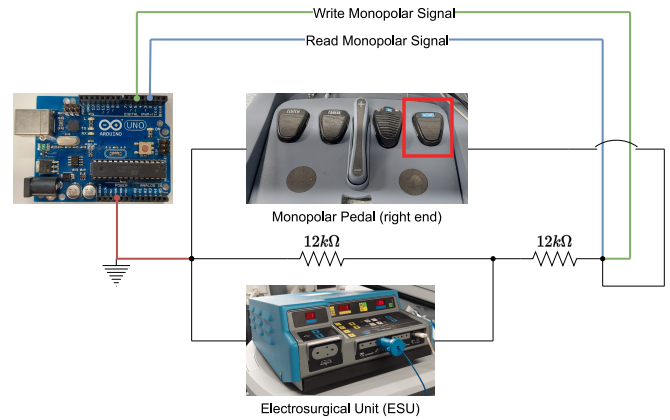


Fig. 2: Circuit of the monopolar pedal and the electro-surgical generator connected to the Arduino Uno Device.

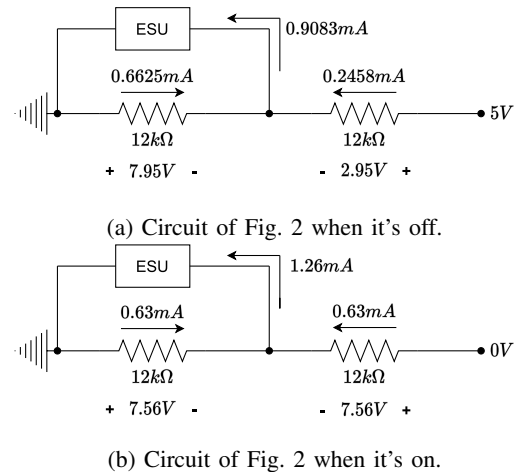


Fig. 3: Circuit of Fig. 2 when the monopolar output is deactivated (a), and when it is activated (b).

as depicted in Fig. 2. The Arduino's write pin defaults to high (5V), and the voltage distribution is depicted in Fig. 3a. In this state, the current remains below the threshold, preventing activation of the monopolar output. The monopolar output is activated either when the Arduino's write pin is triggered (set to low) or when the user presses the pedal, causing the end voltage to short to 0V, thereby surpassing the threshold as illustrated in Fig. 3b.

### C. Kinematic Dataset

In the full da Vinci system, the forward kinematics of the dVRK are deduced from the Setup Joints (SUJs) located at the base of the da Vinci robot. This computation enables the determination of the Patient Side Manipulator (PSM) tip's configuration relative to the Endoscope Camera Manipulator (ECM) tip. It should be noted that the positional variance between the PSM tip and the ECM tip is restricted within a range of  $\pm 5cm$  for translation and falls between  $5 \sim 10$  degrees for orientation, as reported in [21]. Therefore, we introduced a custom calibration for the dVRK using fiducial markers [22].

This approach is influenced by [23], which employs an optical tracking system with custom adapters for instrument

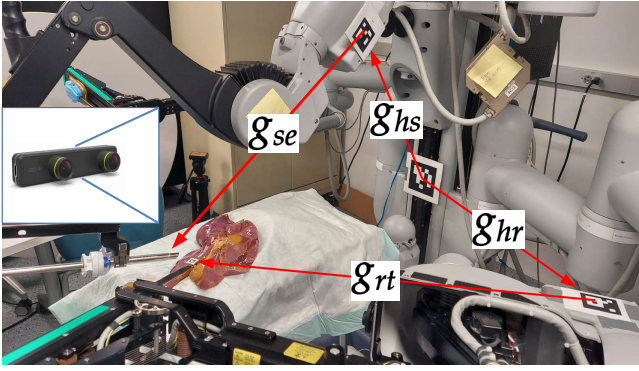


Fig. 4: The setup showing how our custom-calibrated kinematics work. The transformations are shown based on the direction of the arrows and eventually, they are used to find the transformation between the ECM tip and PSM tip.

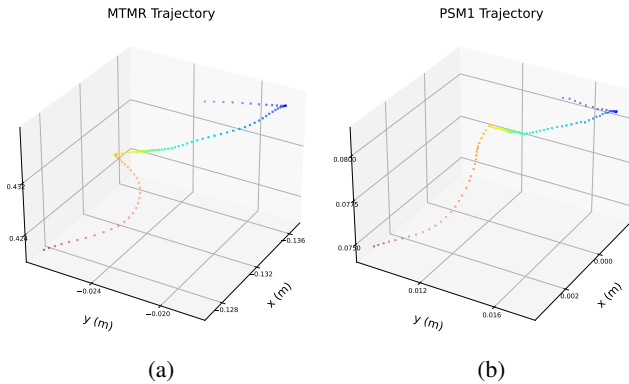


Fig. 5: A sample from the recorded 3D trajectory of the (a) MTMR and (b) PSM1.

tips to calibrate the dVRK. Due to the limited availability of such a system, we opted for the more accessible ArUco markers [24]. Furthermore, we strategically selected base frames for each arm to enhance flexibility, ensuring consistent performance during actual surgical procedures, as illustrated in Fig. 4. More information on the derivation of forward and inverse kinematics can be found in [22].

In Fig. 4, each  $g_{ab}$  represents the transformation (homogeneous matrix) between frames  $A$  and  $B$ . The base frames for the PSM and ECM are denoted by  $R$  and  $S$ , respectively, while  $T$  and  $E$  correspond to their respective instrument tip frames. Once  $g_{rt}$  and  $g_{se}$  are determined, we can establish the relative configuration of the PSM tip with respect to the ECM tip, incorporating the Helper ( $H$ ) frame as depicted in Fig. 4. If there are changes in the locations of the Setup Joints (SUJs), only the transformation between the helper and base frames requires an update. We have:

$$g_{et} = g_{se}^{-1} \cdot g_{hs}^{-1} \cdot g_{hr} \cdot g_{rt} = g_{es} \cdot g_{sh} \cdot g_{hr} \cdot g_{rt} \quad (1)$$

For the PSMs, the dataset encompasses the following information: the transformation from the arm’s base frame to its instrument tip ( $g_{rt}$ ), the transformation from the ECM tip to the PSM instrument tip ( $g_{et}$ ), the joint states (position, velocity, and effort) received from the dVRK, and the joint states (position, velocity, and effort) of the jaw.

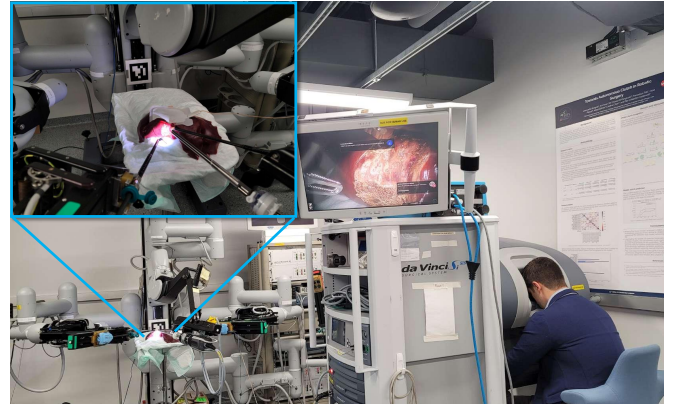


Fig. 6: The environment setup for the ex-vivo cholecystectomy performed by a surgeon.

Regarding the ECM, the dataset includes the transformation from the arm’s base frame to its instrument tip ( $g_{se}$ ), the transformation from the Helper frame to the ECM tip ( $g_{he}$ ), and the joint states (position, velocity, and effort) provided by the dVRK.

For the Master Tool Manipulator (MTM), where the surgeon controls the robot, the raw kinematic data from the dVRK [10], [21] was recorded. This data contains the transformation from the base of each arm to its controller tip, the transformation from the High-Resolution Stereo Video (HRSV) frame (where the console monitor is positioned) to the controller tip, the joint states (position, velocity, and effort) of each arm, and the joint angle of each gripper. The PSM1 is associated with the MTMR (MTM Right), while the PSM2 is paired with MTML (MTM Left). Fig. 5 illustrates a brief motion of the MTMR and the corresponding PSM1.

### III. SURGICAL TASK

#### A. Setup and repetitions

The recordings took place in the setup depicted in Fig. 6, where the surgeon controls the robot with the da Vinci console and executes the assigned task on a pig liver. The data set comprises seven surgeons denoted alphabetically from “A” to “G” who all have experience in surgical robotic cholecystectomy. Each subject performed the task three times. The duration of the task varied according to the difficulty level of the task, influenced by factors such as the decay of the liver. In particular, challenges arose when the color similarity between the liver and gallbladder increased, making it difficult to distinguish between the two objects.

Table II provides details on the recorded dataset for each surgeon. Note that some videos were damaged during compression and were consequently excluded from the dataset. Additionally, occasional shutdowns of the Arduino occurred when a high current was applied to the instrument tip, resulting in the corruption of pedal recordings.

#### B. Description

The surgeons performed the task following the UIC standardized surgical technique for robotic cholecystectomy [25].

Type	Features	Dim	Description (Units)
ECM	Endoscope Tip Cartesian Pose	7	Translation $\{x, y, z\}$ (m), Quaternion $\{x, y, z, w\}$ (rad)
	Local Endoscope Tip Cartesian Pose	7	Translation $\{x, y, z\}$ (m), Quaternion $\{x, y, z, w\}$ (rad)
	Arm Joint State	12	Joint Position $\{\theta(4)\}$ (rad), Joint Velocity $\{\dot{\theta}(4)\}$ (rad/s), Joint Effort $\{\tau(4)\}$ (N)
MTML	Manipulator Tip Cartesian Pose	7	Translation $\{x, y, z\}$ (m), Quaternion $\{x, y, z, w\}$ (rad)
	Local Manipulator Tip Cartesian Pose	7	Translation $\{x, y, z\}$ (m), Quaternion $\{x, y, z, w\}$ (rad)
	Manipulator Joint State	18	Joint Position $\{\theta(6)\}$ (rad), Joint Velocity $\{\dot{\theta}(6)\}$ (rad/s), Joint Effort $\{\tau(6)\}$ (N)
	Manipulator Gripper Joint State	1	Joint Position $\{\theta(1)\}$ (rad)
MTMR	Manipulator Tip Cartesian Pose	7	Translation $\{x, y, z\}$ (m), Quaternion $\{x, y, z, w\}$ (rad)
	Local Manipulator Tip Cartesian Pose	7	Translation $\{x, y, z\}$ (m), Quaternion $\{x, y, z, w\}$ (rad)
	Manipulator Joint State	18	Joint Position $\{\theta(6)\}$ (rad), Joint Velocity $\{\dot{\theta}(6)\}$ (rad/s), Joint Effort $\{\tau(6)\}$ (N)
	Manipulator Gripper Joint State	1	Joint Position $\{\theta(1)\}$ (rad)
PSM1	Instrument Tip Cartesian Pose	7	Translation $\{x, y, z\}$ (m), Quaternion $\{x, y, z, w\}$ (rad)
	Local Instrument Tip Cartesian Pose	7	Translation $\{x, y, z\}$ (m), Quaternion $\{x, y, z, w\}$ (rad)
	Arm Joint State	18	Joint Position $\{\theta(6)\}$ (rad), Joint Velocity $\{\dot{\theta}(6)\}$ (rad/s), Joint Effort $\{\tau(6)\}$ (N)
	Instrument Tip Jaw Joint State	3	Joint Position $\{\theta(1)\}$ (rad), Joint Velocity $\{\dot{\theta}(1)\}$ (rad/s), Joint Effort $\{\tau(1)\}$ (N)
PSM2	Instrument Tip Cartesian Pose	7	Translation $\{x, y, z\}$ (m), Quaternion $\{x, y, z, w\}$ (rad)
	Local Instrument Tip Cartesian Pose	7	Translation $\{x, y, z\}$ (m), Quaternion $\{x, y, z, w\}$ (rad)
	Arm Joint State	18	Joint Position $\{\theta(6)\}$ (rad), Joint Velocity $\{\dot{\theta}(6)\}$ (rad/s), Joint Effort $\{\tau(6)\}$ (N)
	Instrument Tip Jaw Joint State	3	Joint Position $\{\theta(1)\}$ (rad), Joint Velocity $\{\dot{\theta}(1)\}$ (rad/s), Joint Effort $\{\tau(1)\}$ (N)
Pedals	Clutch Pedal State	1	Boolean (True when activated, False otherwise)
	Camera Pedal State	1	Boolean (True when activated, False otherwise)
	Monopolar Pedal State	1	Boolean (False when activated, True otherwise)

TABLE I: List of kinematic variables including the pedal signals. “Local” tip cartesian pose relates the position of the arm’s tip to the arm’s base frame (e.g.  $g_{rt}$  of the PSM). Otherwise, it is the pose of the arm’s tip to its reference frame (the Helper frame, ECM tip frame, and HRSV frame for ECM, PSMs, and MTMs respectively).

	Video	Kinematics	Pedals
<b>A</b>	1	3	3
<b>B</b>	3	3	3
<b>C</b>	3	3	3
<b>D</b>	0	3	3
<b>E</b>	3	3	3
<b>F</b>	3	3	0
<b>G</b>	3	3	3
<b>Total</b>	16	21	18

TABLE II: Recorded dataset distribution from each subject. Some recordings are excluded due to corruption.

It is worth noting that the order of certain steps may potentially vary based on the specific surgical case or anatomical considerations. The primary steps of the procedure are as follows:

- 1) Working area exposure
- 2) Gallbladder neck retraction
- 3) Calot triangle: anterior peritoneal layer opening
- 4) Calot triangle: posterior peritoneal layer opening
- 5) Cystic duct isolation
- 6) Cystic artery isolation
- 7) Cystic duct clipping
- 8) Cystic artery clipping
- 9) Cystic duct and artery division
- 10) Detachment of the gallbladder from the liver
- 11) Specimen retrieval in an Endobag<sup>TM</sup>

However, certain simplifications were applied to the technique mentioned above for this study and within the context of this experimental animal model. In particular, steps 8, 9, and 11 were omitted.

#### IV. PRELIMINARY WORK

##### A. Pedal Prediction

In the context of robotic cholecystectomy, predicting the surgeon’s actions, particularly those involving clutching and manipulating camera pedals, is essential to optimize procedural efficiency and alleviate the surgeon’s cognitive workload. In the current setting, the surgeon takes full control of the robotic system without direct collaboration. Nevertheless, there exists potential to develop a classifier leveraging a comprehensive dataset encompassing the robot’s kinematics and pedal signals. This classifier holds the capability to predict the surgeon’s actions and, subsequently, can be integrated into control systems to guide how the robot should respond.

1) *Dataset Preprocessing*: As indicated in Table II, the robot kinematics ( $\sim 100\text{Hz}$ ) and the console pedal inputs ( $\sim 230\text{Hz}$ ) were captured independently due to their varying frequencies. This necessitated a synchronization process before training classifiers. The initial step involved aligning the datasets by comparing their timestamps and match entries that exhibited a discrepancy within a threshold of  $\varepsilon = 0.006\text{s}$ .

Pedal Type	Data Type	Not Pressed	Pressed	Ratio
Clutch	Original	205406	934	220
	Undersampled	18700	934	20
Camera	Original	201125	5216	36
	Undersampled	78240	5216	20

TABLE III: Class distribution before and after undersampling

Models	Evaluation metrics	Clutch	Camera
AdaBoost	Precision	0.8252	0.9104
	F1 score	0.7540	0.9145
	Recall	0.6941	0.9187
NN	Precision	0.8209	0.9230
	F1 score	0.6688	0.7467
	Recall	0.5354	0.6270
Random Forest	Precision	0.8726	0.9117
	F1 score	0.8379	0.9177
	Recall	0.8059	0.9137
L-GBM	Precision	0.8503	0.9147
	F1 Score	0.8427	0.9256
	Recall	0.8353	0.9367

TABLE IV: Accuracy, Recall, and F1 scores of each model measured on the test set.

Subsequently, to ensure a uniform data quantity, the kinematics data, which was recorded at a lower frequency, underwent interpolation to match the volume of pedal data.

Upon activating the clutch or the camera pedal, the orientations of both the robot arms (PSMs or ECM) and the manipulators (MTMs) are locked in place. However, during this state, the manipulators retain the ability to move while the positions of the da Vinci arms remain stationary. Consequently, we used a sliding window of 20 sequential instances ( $\sim 0.6s$ ) and measured the travel distance associated with the Cartesian translations of the arms and the manipulators. These calculated distances served as the input features for the classifiers, reflecting their distinct behaviors and constraints in response to pedal activation.

The labels for the selected features, which correspond to the pedal signal, exhibit imbalance as highlighted in Table III. This imbalance stems from the pedals being idle (unpressed) predominantly during the procedure. To mitigate the model’s potential bias towards the majority class, we experimented with various ratios for balancing the classes, *True* when the pedal is pressed and *False* otherwise, ranging from 2 to 30, with increments of 2. Through this process, we determined that a ratio of 20 produced the most favorable outcomes in model performance metrics.

2) *Trained Classifiers*: The Random Forests (RF) [26], Adaptive Boosting (AdaBoost) [27], and Feedforward Neural Networks (FNN) [28] classifiers employed in this study are analogous to those introduced in [29]. However, the models have been specifically tuned for binary classification. Furthermore, the structure of the FNN consists of an input layer ( $n_0$ ) sized according to the input characteristics, followed by two fully connected layers ( $n_1, n_2$ ), where the number of neurons is proportional to the size of the previous layer ( $n_1 = 2 \cdot n_0, n_2 = 2/3 \cdot n_1$ ). The final layer ( $n_f$ ) has 1 output

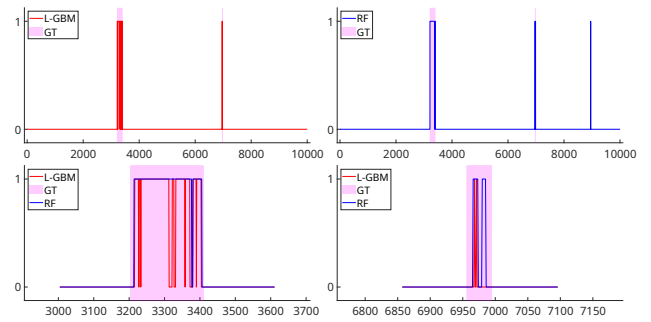


Fig. 7: Models evaluation on the total dataset. The top figures show the predictions from two models (L-GBM and Random Forest). The bottom figures present a zoomed view of the top figure where the clutch was activated.

to function as a binary classifier.

Furthermore, we incorporated a novel classifier, the Light Gradient Boosting Machine (L-GBM) [30]. In L-GBM, decision trees are sequentially added, each tree correcting errors from the ensemble of preceding trees. Unlike conventional gradient boosting, L-GBM directly minimizes the loss function. Designed for distributed and efficient training on large datasets, it is well-suited for applications with resource constraints. L-GBM is distinguished for its leaf-wise growth strategy, effective handling of categorical features, and parallel/distributed training capabilities.

3) *Model Evaluations*: The entirety of the preprocessed window-level datasets, as outlined in Table III, has been divided into training and test sets, allocated at proportions of 80% and 20%, respectively. The overall performance of each trained model on the window is described in Table IV, including the precision, recall, and F1 score.

We considered accuracy at the signal level to further assess model performance beyond window-level metrics. Accordingly, we excluded one of the pedal-kinematic procedures outlined in Table II from the dataset. From Table IV, the RF and the L-GBM outperformed FNN and AdaBoost for predicting clutch. Thus, we selected these models for signal-level performance evaluation. In Fig. 7, we exhibited a trade-off between the model’s sensitivity and its propensity to generate false positives. RF was more stable across long clutch periods but predicted a false clutch at the end of the dataset. In contrast, L-GBM showed precise clutch activation predictions but was unstable over prolonged clutch activations. Further processing could resolve this limitation, such as the voting technique [31]. This method introduces fixed time delays depending on the voting buffer size; however, it enhances the accuracy and reduces short-term false transitions.

## B. Training Tissue Segmentation Models

To automate partial aspects of robotic cholecystectomy, the robot must recognize and keep track of the tissues during the procedure. Currently, there is a notable scarcity of datasets specifically designed for such research. However this new dataset, in contrast to existing ones, uniquely captures the

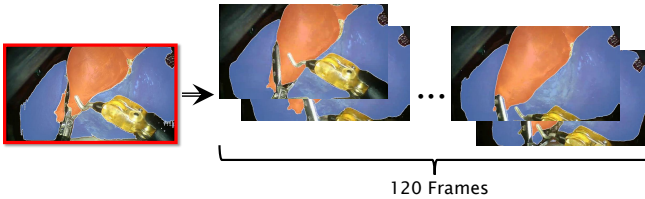


Fig. 8: An example of generating annotations with Track-Anything. Once the initial frame of the video clip (red box) is annotated, Track-Anything starts annotating the rest of the frames.

dynamic changes in tissues during cholecystectomy procedures. Notably, the tissues exhibit a rich diversity in both shape and color. This deliberate inclusion of diverse tissue characteristics is pivotal for training segmentation models, enabling the robot to adeptly recognize and track tissues in real-time during surgical procedures.

1) *Generating segmentation dataset:* In [22], a custom dataset featuring a pig’s liver and gallbladder was generated and it was used to train an object segmentation model called Detectron2 [32]. However, this dataset shares similarities with [12], wherein the arms and the endoscope were manually moved around the object, but no actions were performed on the tissues. Moreover, this elementary dataset was recorded on a single tissue. This posed a significant limitation when it was tested on a new tissue or as the shapes and colors of the tissues changed when the energy was delivered. Consequently, the previously trained model encountered challenges in real-time tissue recognition during the automated procedure. Moreover, the dataset’s size is notably low compared to modern datasets, as video frames had to be downsampled, and each frame had to be manually annotated.

We addressed the limitations inherent in the existing dataset by generating a new dataset, annotated using Track Anything (TA) [33]. Surgical videos from two distinct surgeons (E and F) were utilized where one depicted a nearly ideal cholecystectomy and the other showed a procedure in a challenging surgical environment. This selection aimed to expose the model to diverse surgical scenarios ensuring it learns to accurately handle complex situations encountered in actual surgeries. One limitation of TA is its computational efficiency, which decreases as the number of frames in a video increases. Consequently, we split the videos into short clips with a duration of 2 seconds (equivalent to 120 frames). After annotating the first frame, TA automatically extends the annotations to the remaining frames (Fig. 8). Adjustments to the auto-annotated results could be made if necessary. The training set included a total of 50,149 annotated images (approximately 35 times from [22]).

2) *Training Results:* Table V compares the Average Precision (AP) [34] results for two models, each trained separately on our initial dataset (from [22]) and the recently generated dataset. The models were evaluated on an independent dataset of 1104 images from one of Participant C’s videos. The previous model trained on a controlled dataset shows

	Categories	AP (Box)	AP (Seg.)
Previous Model	Pig Liver	33.3	16.0
	Pig Gallbladder	11.4	10.7
New Model	Pig Liver	62.3	51.9
	Pig Gallbladder	53.9	49.4

TABLE V: The Average Precision (AP) scores (percentages) for each category (Box stands for Bounding Box and Seg. for Segmentation).

markedly limited performance on surgical images indicated by its AP scores. In contrast, the new model, even when trained on just a fraction (two out of 16 videos) of actual surgical footage, demonstrates an improvement over the previous model’s performance. Despite the overall modest scores, the new model’s superiority in this practical context reflects its enhanced capacity to adapt to the complexities of genuine cholecystectomy procedures, hinting at a significant potential for further improvements with comprehensive training on the remaining surgical videos.

## V. CONCLUSION

The current state-of-the-art primarily relies on video-annotated data from well-known datasets. However, a notable gap exists in the incorporation of kinematic data within these datasets, a limitation addressed by recent contributions such as the dataset highlighted in [10]. Despite these advances, challenges persist, including incomplete recordings, imprecise kinematic data due to calibration issues, and the reliance on exercise-based scenarios rather than actual procedures.

Our newly introduced dataset, recorded during ex vivo pseudo-cholecystectomy procedures on pig livers with contributions from seven surgeons, stands out by encompassing patient-side kinematic data, pedal states, and time-stamped videos. Looking ahead, future perspectives in this evolving field involve the development of advanced models to automate various subtasks during surgery, leveraging the unique attributes of data sets like ours.

To demonstrate the practical application of our dataset, we focused on predicting specific subtasks within robotic surgery scenarios. These tasks include predicting clutch and camera pedal activations in conjunction with the kinematics of the robotic arm, console manipulators, and the state of the console pedals. Within this framework, we developed two predictive models: one for clutch usage and another for camera activation, showcasing the dataset’s potential to improve automation and analysis of surgical procedures.

As another example of the utility of the dataset, we studied the segmentation models’ performance, crucial for the robot’s ability to recognize and track tissues during cholecystectomy. The results underscore the significance of our dataset in enhancing the robot’s tissue recognition capabilities. The dynamic changes captured in the tissues during cholecystectomy procedures contribute to improved training models for real-time tissue recognition. This understanding of tissue dynamics lays a foundation for advancing automation in robotic cholecystectomy, where precise tissue identification is paramount.

## REFERENCES

- [1] D. Bouget, R. Benenson, M. Omran, L. Riffaud, B. Schiele, and P. Jannin, "Detecting surgical tools by modelling local appearance and global shape," *IEEE Transactions on Medical Imaging*, vol. 34, no. 12, pp. 2603–2617, 2015.
- [2] T. Ross, A. Reinke, P. M. Full, M. Wagner, H. Kennigott, M. Apitz, H. Hempe, D. M. Filimon, P. Scholz, T. N. Tran, P. Bruno, P. Arbeláez, G.-B. Bian, S. Bodenstedt, J. L. Bolmgren, L. Bravo-Sánchez, H.-B. Chen, C. González, D. Guo, P. Halvorsen, P.-A. Heng, E. Hosgor, Z.-G. Hou, F. Isensee, D. Jha, T. Jiang, Y. Jin, K. Kirtac, S. Kletz, S. Leger, Z. Li, K. H. Maier-Hein, Z.-L. Ni, M. A. Riegler, K. Schoeffmann, R. Shi, S. Speidel, M. Stenzel, I. Twick, G. Wang, J. Wang, L. Wang, L. Wang, Y. Zhang, Y.-J. Zhou, L. Zhu, M. Wiesenfarth, A. Kopp-Schneider, B. P. Müller-Stich, and L. Maier-Hein, "Robust medical instrument segmentation challenge 2019," 2020.
- [3] M. Allan, S. Kondo, S. Bodenstedt, S. Leger, R. Kadkhodamohammadi, I. Luengo, F. Fuentes, E. Flouty, A. Mohammed, M. Pedersen, A. Kori, V. Alex, G. Krishnamurthi, D. Rauber, R. Mendel, C. Palm, S. Bano, G. Saibro, C.-S. Shih, H.-A. Chiang, J. Zhuang, J. Yang, V. Igloukov, A. Dobrenkii, M. Reddiboyna, A. Reddy, X. Liu, C. Gao, M. Unberath, M. Kim, C. Kim, C. Kim, H. Kim, G. Lee, I. Ullah, M. Luna, S. H. Park, M. Azizian, D. Stoyanov, L. Maier-Hein, and S. Speidel, "2018 robotic scene segmentation challenge," 2020.
- [4] W.-Y. Hong, C.-L. Kao, Y.-H. Kuo, J.-R. Wang, W.-L. Chang, and C.-S. Shih, "Cholecseg8k: a semantic segmentation dataset for laparoscopic cholecystectomy based on cholec80," *arXiv preprint arXiv:2012.12453*, 2020.
- [5] M. Carstens, F. M. Rinner, S. Bodenstedt, A. C. Jenke, J. Weitz, M. Distler, S. Speidel, and F. R. Kolbinger, "The dresden surgical anatomy dataset for abdominal organ segmentation in surgical data science," *Scientific Data*, vol. 10, no. 1, p. 3, 2023.
- [6] A. P. Twinanda, S. Shehata, D. Mutter, J. Marescaux, M. De Mathelin, and N. Padoy, "Endonet: a deep architecture for recognition tasks on laparoscopic videos," *IEEE transactions on medical imaging*, vol. 36, no. 1, pp. 86–97, 2016.
- [7] Y.-H. Su, K. Huang, and B. Hannaford, "Real-time vision-based surgical tool segmentation with robot kinematics prior," in *2018 International Symposium on Medical Robotics (ISMR)*, pp. 1–6, 2018.
- [8] C. da Costa Rocha, N. Padoy, and B. Rosa, "Self-supervised surgical tool segmentation using kinematic information," in *2019 International Conference on Robotics and Automation (ICRA)*, pp. 8720–8726, IEEE, 2019.
- [9] I. Rivas-Blanco, C. J. Pérez-Del-Pulgar, I. García-Morales, and V. F. Muñoz, "A review on deep learning in minimally invasive surgery," *IEEE Access*, vol. 9, pp. 48658–48678, 2021.
- [10] I. Rivas-Blanco, C. J. P. Del-Pulgar, A. Mariani, G. Tortora, and A. J. Reina, "A surgical dataset from the da vinci research kit for task automation and recognition," in *2023 3rd International Conference on Electrical, Computer, Communications and Mechatronics Engineering (ICECCME)*, pp. 1–6, 2023.
- [11] Y. Gao, S. S. Vedula, C. E. Reiley, N. Ahmidi, B. Varadarajan, H. C. Lin, L. Tao, L. Zappella, B. Béjar, D. D. Yuh, *et al.*, "Jhu-isi gesture and skill assessment working set (jigsaws): A surgical activity dataset for human motion modeling," in *MICCAI workshop: M2cai*, vol. 3, 2014.
- [12] E. Colleoni, P. Edwards, and D. Stoyanov, "Synthetic and real inputs for tool segmentation in robotic surgery," in *International Conference on Medical Image Computing and Computer-Assisted Intervention*, pp. 700–710, Springer, 2020.
- [13] K. A. Cullen, M. J. Hall, and A. Golosinskiy, "Ambulatory surgery in the united states, 2006," 2009.
- [14] A. G. Harrell and B. T. Heniford, "Minimally invasive abdominal surgery: lux et veritas past, present, and future," *The American journal of surgery*, vol. 190, no. 2, pp. 239–243, 2005.
- [15] D. S. Strosberg, M. C. Nguyen, P. Muscarella, and V. K. Narula, "A retrospective comparison of robotic cholecystectomy versus laparoscopic cholecystectomy: operative outcomes and cost analysis," *Surgical endoscopy*, vol. 31, pp. 1436–1441, 2017.
- [16] G. Bradski, "The OpenCV Library," *Dr. Dobb's Journal of Software Tools*, 2000.
- [17] Z. Zhang, "A flexible new technique for camera calibration," *IEEE Transactions on Pattern Analysis and Machine Intelligence*, vol. 22, no. 11, pp. 1330–1334, 2000.
- [18] J. Bouguet, "Matlab camera calibration toolbox," 2000.
- [19] Open Source Robotics Foundation, "Robot operating system."
- [20] R. Smith, "An overview of the tesseract ocr engine," in *Ninth International Conference on Document Analysis and Recognition (ICDAR 2007)*, vol. 2, pp. 629–633, 2007.
- [21] P. Kazanzides, Z. Chen, A. Deguet, G. S. Fischer, R. H. Taylor, and S. P. DiMaio, "An open-source research kit for the da vinci surgical system," in *IEEE Intl. Conf. on Robotics and Auto. (ICRA)*, (Hong Kong, China), pp. 6434–6439, 2014.
- [22] K.-H. Oh, L. Borgioli, M. Zefran, L. Chen, and P. C. Giulianotti, "A framework for automated dissection along tissue boundary," *arXiv preprint arXiv:2310.09669*, 2023.
- [23] O. Özgüner, T. Shkurti, S. Huang, R. Hao, R. C. Jackson, W. S. Newman, and M. C. Çavuşoğlu, "Camera-robot calibration for the da vinci robotic surgery system," *IEEE Transactions on Automation Science and Engineering*, vol. 17, no. 4, pp. 2154–2161, 2020.
- [24] S. Garrido-Jurado, R. Muñoz-Salinas, F. Madrid-Cuevas, and M. Marín-Jiménez, "Automatic generation and detection of highly reliable fiducial markers under occlusion," *Pattern Recognition*, vol. 47, no. 6, pp. 2280–2292, 2014.
- [25] P. Giulianotti, E. Benedetti, and A. Mangano, *The Foundation and Art of Robotic Surgery*. McGraw-Hill Education, 2024.
- [26] L. Breiman, "Random forests," *Machine learning*, vol. 45, pp. 5–32, 2001.
- [27] Y. Freund and R. E. Schapire, "A decision-theoretic generalization of on-line learning and an application to boosting," *Journal of computer and system sciences*, vol. 55, no. 1, pp. 119–139, 1997.
- [28] I. Goodfellow, Y. Bengio, and A. Courville, *Deep Learning*. MIT Press, 2016. <http://www.deeplearningbook.org>.
- [29] Z. Rysbek, K.-H. Oh, and M. Zefran, "Recognizing intent in collaborative manipulation," in *Proceedings of the 25th International Conference on Multimodal Interaction, ICMI '23*, (New York, NY, USA), p. 498–506, Association for Computing Machinery, 2023.
- [30] G. Ke, Q. Meng, T. Finley, T. Wang, W. Chen, W. Ma, Q. Ye, and T.-Y. Liu, "Lightgbm: A highly efficient gradient boosting decision tree," in *Advances in Neural Information Processing Systems* (I. Guyon, U. V. Luxburg, S. Bengio, H. Wallach, R. Fergus, S. Vishwanathan, and R. Garnett, eds.), vol. 30, Curran Associates, Inc., 2017.
- [31] H. A. Varol, F. Sup, and M. Goldfarb, "Multiclass real-time intent recognition of a powered lower limb prosthesis," *IEEE Transactions on Biomedical Engineering*, vol. 57, no. 3, pp. 542–551, 2010.
- [32] Y. Wu, A. Kirillov, F. Massa, W.-Y. Lo, and R. Girshick, "Detectron2." <https://github.com/facebookresearch/detectron2>, 2019.
- [33] J. Yang, M. Gao, Z. Li, S. Gao, F. Wang, and F. Zheng, "Track anything: Segment anything meets videos," 2023.
- [34] T.-Y. Lin, M. Maire, S. Belongie, L. Bourdev, R. Girshick, J. Hays, P. Perona, D. Ramanan, C. L. Zitnick, and P. Dollár, "Microsoft coco: Common objects in context," 2014.